

Thermal shock fabrication of ion-stabilized perovskite and solar cells

Yifei Kang^{1}, Anran Wang^{1*}, Rong Li^{1*}, Yilong Song¹, Xinjiang Wang², Hanming Li¹, Weiqing Xu,¹ Lijun Zhang² and Qingfeng Dong¹ †*

¹ State Key Laboratory of Supramolecular Structure and Materials, College of Chemistry, Jilin University, Changchun 130012, China

² Key Laboratory of Automobile Materials of MOE and School of Materials Science and Engineering, Jilin University, Changchun 130012, China

*These authors contributed equally to this work.

† Correspondence author. Email: qfdong@jlu.edu.cn

Here we show a highly crystalline perovskite grain structure with compressed surface lattice realized by a thermal-shocking fabrication. The strained perovskite grain structure is stabilized by Cl⁻-reinforcing surface lattice and show enhanced bonding energy and ionic activation temperature, which contributes to hysteresis-free operation of perovskite solar cells (PSCs) at much higher temperature up to 363 K in thermal-shocking processed MAPbCl_xI_{3-x} (T-MPI). The PSCs can be fabricated by a high-speed fully-air-process without post annealing based on scalable bar-coating technique. Both high efficiency and stability are achieved in T-MPI PSC with a power conversion efficiency (PCE) up to 22.99% and long-term operational stability with T₈₀ lifetime exceeding 4000 hours.

Keywords: perovskite solar cells, ion migration, thermal-shocking

This article has been accepted for publication and undergone full peer review but has not been through the copyediting, typesetting, pagination and proofreading process, which may lead to differences between this version and the [Version of Record](#). Please cite this article as [doi: 10.1002/adma.202203166](https://doi.org/10.1002/adma.202203166).

This article is protected by copyright. All rights reserved.

1. Introduction

Organic-inorganic halide perovskite (OIHP) has a rocketing development in optoelectronic device^[1-7] in the past decade with the power conversion efficiency (PCE) approaching their commercialized counterparts. Additionally, the breakthroughs in device structure design, composition or additive engineering^[8] and encapsulation^[9] bring fast development in device stability under UV, thermal and humid aging conditions.^[10, 11] However, there are still challenges in the intrinsic ionic stability in both device and materials due to the intrinsic ionic nature of perovskite compared with traditional inorganic semiconductors. Severe temperature-amplified hysteresis effect^[12] and materials decomposition or phase segregation are observed in almost all types of efficient metal halide perovskites, including methylamine (MA),^[13] mixed^[14] and even all-inorganic Cs cations-based perovskites,^[15] so that it is still challengeable to achieve high efficiency and stable operation of PSCs simultaneously when the bias and high temperature are involved in long-term real working condition. The low ionic migration activation energy (E_a) resulting in a low ionic activated temperature near room temperature (RT) is believed to be the origin of ion migration effect of OIHP devices under working bias.^[16] Huang *et al.*^[17] reported that in bulk single-crystalline $\text{CH}_3\text{NH}_3\text{PbI}_3$ (MPI), the E_a is 0.624 eV under the electric field of 0.4 V/ μm in dark and the ionic activated temperature is 276 K, while the E_a further decreased to 0.338 eV under illumination. Meanwhile, the E_a would further deteriorate in polycrystalline perovskite thin films to almost half of that in single crystals due to the much lower E_a in amorphous or low-crystallized grain boundaries (GBs). These regions were proved as major ion migration pathways rather than in bulk.^[12, 18] Most critically, there is always much higher working temperature and stronger illumination in real working condition of OIHP devices, which would further boost the ion migration effect and thus accelerate the decomposition of perovskites.^[19, 20]

Great efforts have been made from both materials and devices to mitigate the bias induced ionic instability of perovskites. On one hand, improving the crystallinity of perovskite thin films towards single crystal is one efficient strategy to reduce ion migration pathways by suppressing the ratio of GBs^[21] and high operational stability is reported in co-planar structured MAPbI₃ single crystal devices.^[22] On the other hand, most efficient OIHP devices are based on polycrystalline thin film structures, thus composition engineering to enhance intrinsic stability of OIHP materials, such as introducing low-dimensional^[23] or inorganic structures,^[24] and interfaces engineering for defects passivation of GBs^[25-27] are the main strategies to optimize the stability of PSCs. However, the carrier transport and ionic properties are still limited by the intrinsic bulk grain with soft lattice.^[26] So it is imperative to ameliorate the intrinsic ionic stability of OIHPs under operation condition without compromising device efficiency and solution-processable advantages.

Recently, it is found that strain engineering showed potential to provide another pathway to stabilize perovskite materials as well as devices by inhibiting ion migration^[28-30]. However, it is still controversial whether the mechanical interaction between the thin interface layer and the non-epitaxial perovskite layer offsetting the residual strain. Meanwhile, the annealing-related modification process will generate additional disturbance about the residual strain, making it hard to clarify the strain-related effect in efficient PSCs.^[28]

Here, an air-processed thermal-shocking (TS) assisted bar-coating process is developed to fabricate highly crystalline perovskite polycrystalline thin films without requirement of post-annealing. Compressed surface lattice structure like tempered-glass is formed and stabilized during the synchronous flash thermal sintering-quenching (SFTSQ) process. The flash TS fabrication instantaneously solidifies the liquid film with Cl⁻ kinetically trapped in surface lattice, which dramatically enhances the E_a value of film to that in single crystal regardless of in-plane or out-of-plane direction. The thermal-shocking processed MAPbCl_xI_{3-x} (T-MPI) shows higher phase stability, smaller surface lattice space and higher

bonding energy, which significantly enhances the ionic activation temperature and contributes to hysteresis-free operation of PSCs at high temperatures up to 363 K with high operational stability. Power conversion efficiency (PCE) approaching ~23% with a low nonradiative voltage loss of 109 mV is achieved after passivation and enables T-MPI PSC to work as a highly stable LED. In addition, T-MPI device also shows environment and thermal-shocking stability, enabling perovskite films can be fabricated under high relative-humidity (RH) up to 90% in air for scalable device fabrication.

2. Results and discussion

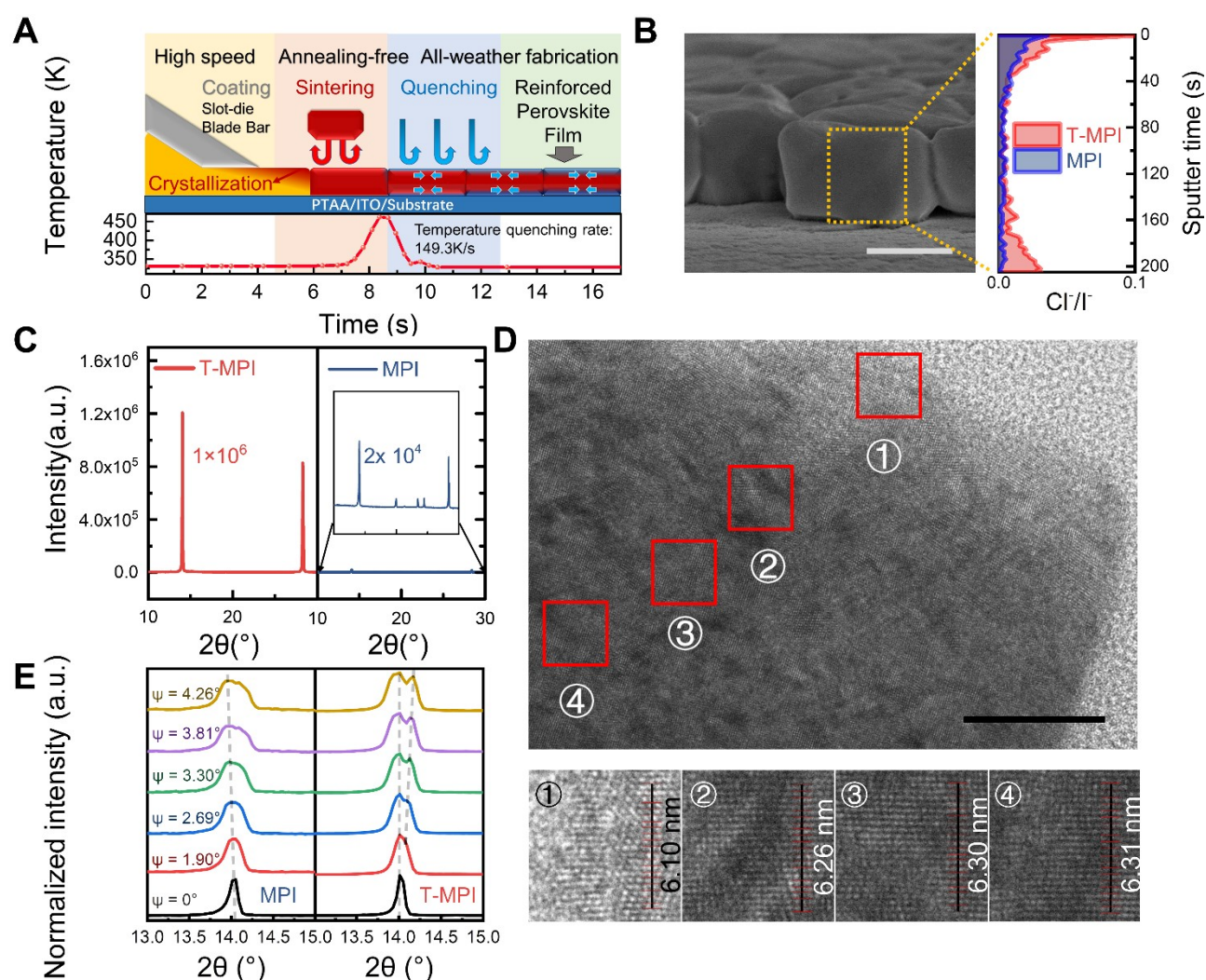


Figure 1. Preparation of T-MPI films and structural characterizations

(A) Schematic diagram of synchronous flash thermal sintering-quenching (SFTSQ) process. Temperature variation on the corresponding substrate surface recorded by a high-precision IR temperature sensor with fast response. (B) Cross-sectional SEM image of T-MPI film and TOF-SIMS spectra of Cl⁻/I⁻ ions in the T-MPI and MPI film. Scale bar, 500 nm. (C) XRD patterns of MPI and T-MPI films, the inset is the MPI XRD pattern enlarged by 20 times. (D) TEM image of the stand-free T-MPI partial grain. Scale bar, 20 nm. The bottom picture showed high resolution TEM images of lattice from surface into the interior of the T-MPI grain (1-4). (E) XRD pattern with different tilt angle ψ values (0°-4.26°) for T-MPI and control film.

In order to incorporate and stabilize the compressively strained surface, perovskite films were fabricated by hydrochloric acid-assisted TS strategy (Figure 1A). First, we introduced hydrochloric acid into precursor solution^[31-33] to enable a directly crystallization of perovskite grains by eliminating the formation of acicular solvate, which was evidenced by in-situ observation of crystallization process (Figure S1) and dynamic light scattering (Figure S2). This direct solvent volatilization process is the basis for flash crystallization since the saturated vapor pressure of solid intermediates is very low. Then, the wet precursor film underwent a flash thermal shocking process while spread, which was instantly heated up to above 453 K during the flash high temperature by a highly localized heat source enabling the solvent to evaporate completely (Figure S3), so that the liquid film real-timely transferred into a metallic-lusted perovskite films within 0.1 s timescale without requirement of post annealing. Right after that, just-fully crystallized film was rapidly cooled via an instantaneous quenching by air cooling with an extremely high cooling rate up to 149.3 K/s (Figure 1A). The optimization of the quenching process was shown in Figure S4. The formation of high-quality films was benefited from the air blowing effect^[34] as well as the directly crystallization process with higher nucleation and growth rate caused by the instantaneous supersaturation during the accelerating solvent volatilization process.

The optimized crystallization process contributed to highly crystalline large grains completely penetrating the entire perovskite film (Figure 1B) with extremely narrow full width at half maximum as low as 0.08° in the X-ray diffraction (XRD) (Figure 1C), which showed highly oriented (100) and (200) diffraction peaks with an extremely high Lotgering factor at $\{c00\}$ orientation of 98.28% towards that in single crystal with significantly stronger intensity than regular MAPbI₃ films. This highly ordered (100) lattice plane packing is believed to have a lower defect density^[35] and contributes to higher charge transport properties^[36] as well as stronger hydrophobicity.^[37] Apart from this, the high crystallinity of grain lattice structures can be clearly observed by transmission electron microscope (TEM) with little amorphous region even at grain boundary (Figure 1D).

Tilt angle ψ -dependent XRD measurement was taken to analyze the changes in residual strain (Figure 1E). We chose a smaller tilt angle range because the larger tilt angle might make the precise peak position unrecognizable and could not represent the interplanar spacing distribution of most grains for a highly oriented film. The results showed that as the ψ increased, the (100) peak position of the control film shifted to lower angles, showing that it was subjected to the tensile strain on account of the mismatch of the thermal expansion coefficient, which would have an unfavorable effect on optoelectronic properties and stability of devices.^[38] While the peak position of the T-MPI film did not shift, showing that the annealing-free process effectively eliminated the tensile strain from the substrate. In addition, a new peak appeared at higher angle and gradually shifted to the right, indicating that the local lattice may have compressive strain (detailed discussions were shown in the supplementary discussion 1).

The surface lattice structure in a single grain was evaluated by calculating lattice spacing measured across the grain in different regions as shown in Figure 1D. The interplanar spacing of the region near the interior was around 3.15 Å, while the interplanar spacing near the edge was 3.05 Å. In the simulated lattice fringes pattern obtained from the corresponding real

space lattice via the Fast Fourier Transform (FFT) and inverse FFT algorithm, it can be seen more clearly that the edge area had smaller interplanar spacing (Figure S5). In order to exclude the lattice damage caused by the electron beam, the lattice spacing of polished film was also measured as a reference (Figure S6). As a strong contrast, the lattice spacing from the surface to inside was almost the same. This atomistic-scale imaging directly evidenced the compressed skin lattice structure in stand-free grains which eliminated the influence of the interaction between the substrate and the grains.

To understand the formation of surface compression structure, time-of-flight secondary ion mass spectrometry (TOF-SIMS) depth profiles were taken to observe the depth-dependent composition. T-MPI film showed significantly more chloride ion at skin area and the concentration gradient of Cl^- changed more drastically from the outside to the inside compared with the reference film with the same amount of Cl^- added as indicated by the depth-dependent distribution of Cl/I shown in Figure 1B, while there was no MAPbCl_3 diffraction peak at $2\theta = 15.8^\circ$ and MACl diffraction peak at $2\theta = 17.5^\circ$ in XRD (Figure S7). These results evidenced that the Cl^- kinetically trapped in the surface lattice and retained this uneven distribution. We speculated that the flash film forming process during thermal quenching froze volatile ions and enabled the system to enter a non-equilibrium state. The kinetic control of the thermodynamic mixing^[39] makes it possible to form uneven distribution of Cl^- in doped crystalline solid solution with entropy gain^[40, 41] and higher energy barrier,^[42] which maintained the reinforced surface with compressed and denser lattice structure, just as that was observed in TEM images (detailed discussions were shown in the supplementary discussion 2). Furthermore, this can also explain why the chlorine content was also gradually increasing in the region near the bottom interface which was close to the cooler substrate and cooled more quickly.

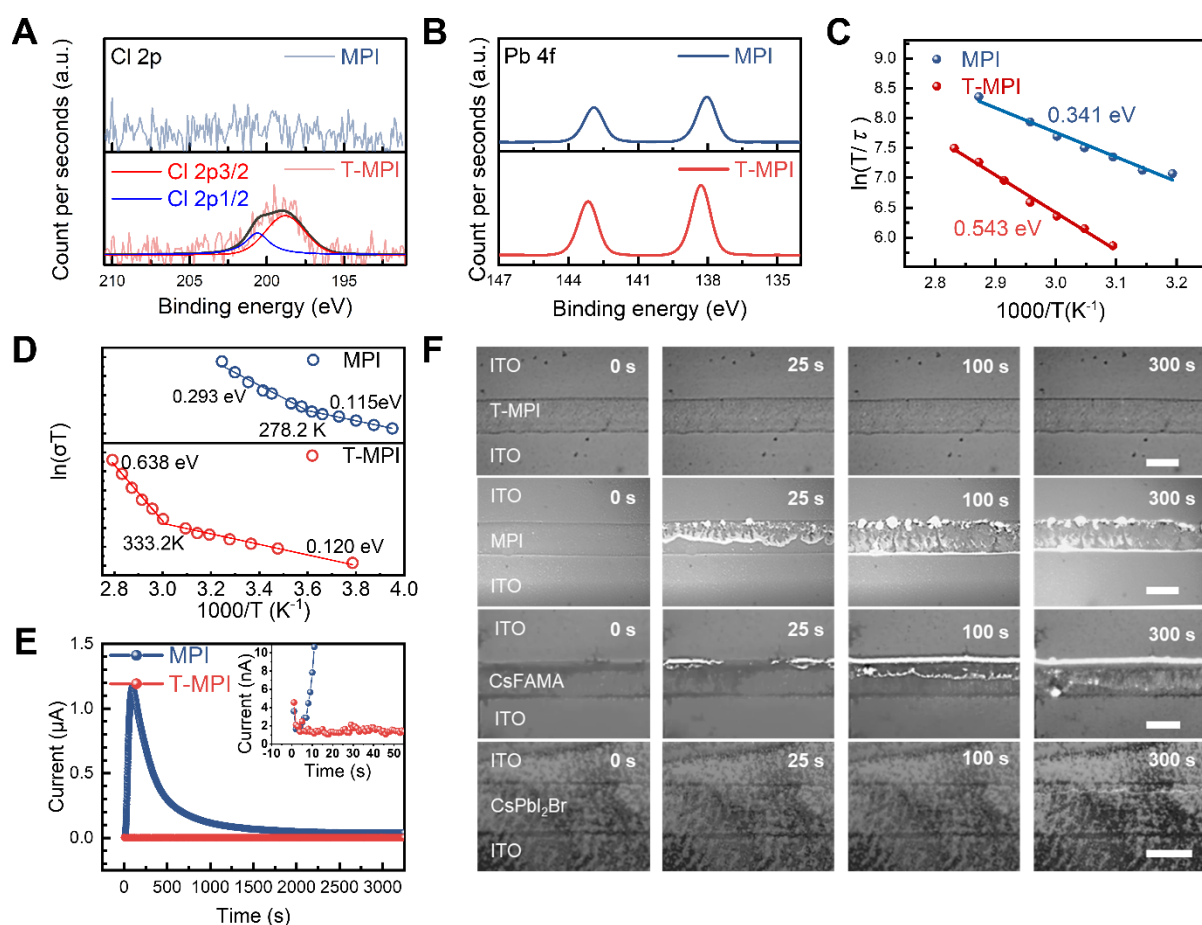


Figure 2. Surface chemical state and ion migration characterization of MPI and T-MPI films.

(A) Chlorine XPS spectrum of T-MPI and MPI films. (B) Lead XPS spectrum of T-MPI and MPI films. (C) Temperature-dependent T/τ Arrhenius plots. (obtained by linear fitting of data points). The calculated E_a of the MPI film and T-MPI film are 0.341 eV and 0.543 eV, respectively. ITO/Au/perovskite/Au vertical structured devices were used for E_a measurement. (D) Temperature-dependent conductance plot of MPI (top) and T-MPI (down) lateral structure devices (Au/perovskite/Au). (E) Lateral structure devices (Au/perovskite/Au) dark current response at 2 V/μm electric polarization. The inset showed detailed dark current response at a smaller time scale. (F) Characterization of ion migration speed in lateral structure device (ITO/PVK/ITO) under illumination (13.8 mW/cm²) and electric polarization (1 V/μm). CsFAMA represented Cs_{0.02}MA_{0.6}FA_{0.38}PbI_{2.975}Br_{0.025}. Scale bar, 50 μm.

To gain more insight into surface chemical state changes of perovskite films, X-ray photoelectron spectroscopy (XPS) was used to characterize the top surface chemical state of perovskite films. Figure 2A showed that in the T-MPI film, the binding energy at 198.7 and 200.5 eV were assigned to $2p_{3/2}$ and $2p_{1/2}$ of Cl^- , respectively, while no peaks were observed here for the regular MAPbI_3 since the effective doping amount of the conventional method was too low to be detected. Correspondingly, the binding energy of Pb^{2+} in T-MPI shifted to 143.15 and 138.30 eV compared with the binding energy at 142.90 and 138.05 eV assigned to $4f_{5/2}$, $4f_{7/2}$ of Pb^{2+} in regular MAPbI_3 , respectively (Figure 2B), after calibrating the peak position with the C element (Figure S8). In addition, these results indicated that the outer electron density of Pb decreased, proving a stronger chemical bonds were formed due to the lattice doping of Cl^- with smaller radius in the SFTSQ process. Moreover, The Cl to Pb atomic ratio calculated by XPS was 0.33, which was close to the surface Cl content obtained from the TOF-SIMS spectrum. The metal-halide bond strength will significantly affect the mechanical properties of the perovskite.^[43, 44] Therefore, we tested the mechanical properties of the film surface with a nanoindenter (Figure S9). The hardness at surface of the T-MPI film increased from 0.74 ± 0.17 GPa to 0.88 ± 0.11 GPa compared to the MPI film, which was related to the formation of more Pb-Cl bonds and the solid solution strengthening effect.

The effect of global strain and micro strain management on E_a in the out-of-plane direction was evaluated in indium tin oxide (ITO)/Au/perovskite (PVK)/Au vertical structured devices.^[35, 45] Figure S10 showed the typical temperature-dependent instantaneous reverse current decay lifetime when the electric field was suddenly interrupted. The E_a of T-MPI device reached 0.543 eV, which was significantly higher than the 0.341 eV in reference device (Figure 2C). Furthermore, E_a in the in-plane direction was also evaluated based on Nernst-Einstein relationship in the Au/PVK/Au lateral-structure devices. As shown in Figure 2D, the ion migration of the reference device started at 278 K, while there was a significant enhancement to ~ 333 K in T-MPI devices. Moreover, the E_a of T-MPI device in

lateral direction was as high as 0.638 eV, which was approaching that in MAPbI₃ single crystal and much higher than that in regular MAPbI₃ with 0.293 eV.^[17] These suggested that ion migration was effectively suppressed regardless of in horizontal or vertical direction. Suppression of ion migration effect was also evaluated by tracking the dark current under electric field via applying 2 V/ μ m bias in lateral devices (Figure 2E)^[46]. There was an obvious deceleration and accumulation process of migrating ions at the electrode in control films implied by the rapid variational ionic current which could not reach a stable level even after 40 minutes. While the current of T-MPI film rarely changed with significantly suppressed current, suggesting ion migration was effectively inhibited. The main origin of the significantly enhanced ionic stability was believed to benefit from the surface-compressed structure caused by the incorporation of Cl⁻ in surface lattice which enhanced the binding energy of the surface lattice, restricted the path of ion migration, and increased the ion migration activation energy. Reported DFT calculations also suggested that surface Cl⁻-doped MAPbI₃ had higher decomposition energy^[42] and I vacancy formation energy.^[47] Besides that, prominently enhanced orientation and elimination of residual tensile stress from the substrate also enabled ion migration to be suppressed.^[35, 38]

microscopic morphology tracking for films based on T-MPI as well as most studied perovskite compositions including all-MA, mixed or all-inorganic cations-based perovskites (Figure 2F). The measurement was taken by tracking contrast variation in transmittance of the films under illumination with 1 V/ μ m electrical field applied.^[15, 25] In regular MAPbI₃ film, the morphology rapidly varied just in the first few seconds, while a visibly slower migration effect was observed in mixed perovskite film (Cs_{0.02}MA_{0.6}FA_{0.38}PbI_{2.975}Br_{0.025}), however, serious degradation still occurred in only tens of seconds. All-inorganic CsPbI₂Br film showed better ionic stability as predicted, but a bright thread was still observed after about 300 s, indicating there was still ion migration even in all inorganic perovskite films even at RT under illumination. As a striking contrast, near 1000 times lowered ion migration

rate was observed in T-MPI films than regular MAPbI₃ films with rarely changes in 1800 s (Figure S11) under the same condition. After increasing the electric field intensity to 2 V/ μ m, the T-MPI films also showed an effectively suppressed migration speed with little changes observed after 4000 s (Figure S12).

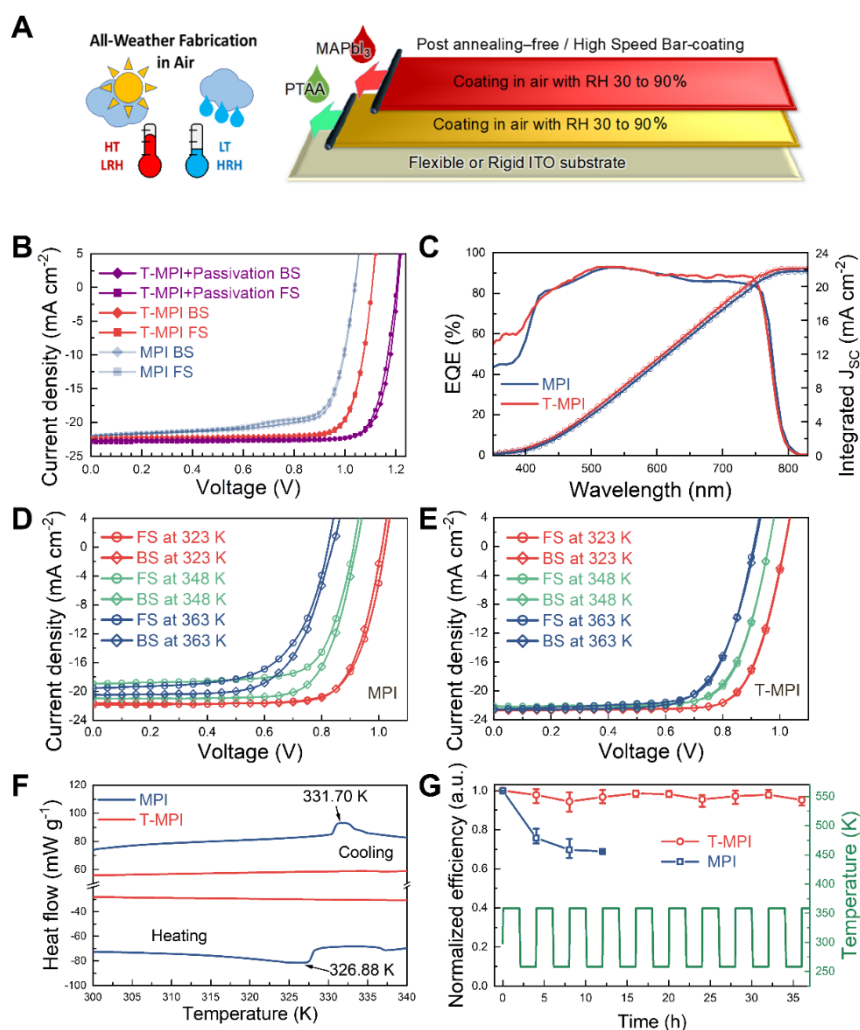


Figure 3. Device preparation and performance characterization

(A) Schematic diagram of an all-weather device fabrication process using the SFTSQ scalable coating method. (B) J - V characteristics of T-MPI and control devices, obtained from backward and forward scans under simulated AM 1.5G illumination at 100 mW/cm². The detailed parameters are listed in Table S1. (C) External quantum efficiency (EQE) curves of

MPI, T-MPI PSCs. (D-E) Temperature-dependent J - V curves of MPI (D) and T-MPI (E) based PSCs. BS stands for backward scan, and FS stands for forward scan. (F) Differential scanning calorimeter (DSC) plot of MPI and T-MPI PSCs. (G) Thermal cycling stability test of MPI and T-MPI devices referred to the *ISOS-T-2I* protocol.^[48]

Ion migration effect under operational conditions was subsequently examined by in-situ

Enhanced charge transport properties were also observed in T-MPI films beyond better stability. Space charge-limited current (SCLC) method was used to study carriers transport properties and defects properties of films (Figure S13). The measured defects concentration decreased markedly from $2.74 \times 10^{15} / \text{cm}^3$ to $6.90 \times 10^{14} / \text{cm}^3$, indicating the suppressed defect states density. The time-resolved photoluminescence (TRPL) spectrum results (Figure S14) showed the PL lifetime increased more than six times, revealing fewer non-radiative transition channels.^[49] These showed that the Cl^- -doped denser surface lattice-structure with enhanced orientation ameliorated the charge transport properties in perovskite films while constructively suppressing ion migration.

The highly crystallized T-MPI enabled high performance PSCs by the scalable all-bar-coating process, which was evaluated by the well-studied inverted planar device structure of ITO/Poly[bis(4-phenyl)(2,4,6-trimethylphenyl)amine](PTAA)/PVK/ C_{60} /bathocuproine (BCP)/Cu (Figure 3A). Even though there was no further passivation layer, the T-MPI device showed an open-circuit voltage (V_{oc}) of 1.10 V, a short-circuit current density (J_{sc}) of 22.29 mA/cm^2 and a high fill factor (FF) of 82.02%, yielding a PCE of 20.37% in forward scanning and 20.11% efficiency in backward scanning with little hysteresis (Figure 3B). We considered the increase in V_{oc} came from the highly ordered (100) lattice plane packing which reduced the defect density^[21, 47] and enhanced charge transport properties.^[36] Besides that, Cl^- -dope also enhanced the carrier recombination lifetime.^[50] The efficiency of 1 cm^2 large-area device was also close to 20%, showing a good scalability of the SFTSQ method

(Figure S15). The integrated current density from external quantum efficiency (EQE) curve was 22.12 mA/cm^2 , which coincided well with J_{SC} (Figure 3C). Detailed performance parameters including steady-state output efficiency, devices statistical efficiencies and module efficiency were shown in Tab. S1 and Figure S16A-C. In this work, the unpassivated films were used because they can be accurately evaluated the intrinsic properties and stability without interference by further surface interaction.

By simply introducing a choline chloride interfacial layer for further passivating surface defects and suppressing the nonradiative recombination channel,^[51] an ultra-low voltage loss with V_{OC} of 1.21 V and astoundingly high FF up to 83.66% can be achieved synchronously with a PCE of 22.99% in backward scan and 1.20 V, 83.48% FF, 22.98% PCE in forward scan with inappreciable hysteresis and up to 22.50 mA/cm^2 integrated current density from EQE curve (Figure 3B, S17), which enabled scalable-processed inverted PSCs to approach a competitive efficiency to that by spin-coating. Recent progress of scalable-processed PSCs was summarized in Tab. S2. By comparison, the reference device showed an V_{OC} of 1.04 V, a J_{sc} of 22.00 mA/cm^2 , FF of 75.31% and a PCE of 17.23%. In addition, the T-MPI PSC device after introducing interfacial layer can act as a solar cell-structured LED without further structure optimization and showed 3.8% EQE_{EL} with electroluminescence (EL) peak position of 775 nm and no peak position shift from 1.2 V to 2.2 V (Figure S18-19). From the EQE_{EL} , EQE, J_{SC} , and V_{OC} of the T-MPI PSC, the nonradiative voltage loss can be calculated as low as 109 mV (Figure S18-20), which was in the forefront of the reported PSCs.

Temperature-dependent J - V characteristics of MAPbI₃-based PSCs without extra interfacial passivation was further investigated under 1 Sun illumination to simulate real high temperature operational condition of PSCs to evaluate the influence from ion migration effect under illumination and increased temperature as well as induced thermal stress.^[15] The V_{OC} linear decreased with increasing temperature for both reference and T-MPI devices, which was determined by the inherent physical properties of the semiconductor.^[52] The traditional

PSCs strongly affected by temperature with significantly increased hysteresis factor even though devices performed well at RT (Figure 3D). Moreover, there was a faster V_{OC} drop as well as a significant attenuation of the J_{SC} and FF (Figure S21). In contrast, T-MPI devices showed marginal hysteresis with ten times lower hysteresis factors than regular PSCs, even when the temperature increased to 363 K (Figure 3E, S22). There were almost rare changes in J_{SC} and FF at different temperatures, indicating effectively suppressed ion migration even in real working condition with full Sun illumination and attendant bias and heating effect, which had proved to be a main reason for hysteresis effect in PSCs. It should be noted that from the results of Differential Scanning Calorimetry (DSC), the T-MPI sample had no phase change in the range of 273-383 K (Figure S23), which eliminating the phase transition (Figure 3F) induced instability. This may be due to the Cl^- doping or/and DMA^+ doping produced by the hydrolysis of DMF under acidic conditions,^[53] which made the tolerance factor closer to 1 and remaining cubic phase.^[54-56] In order to exclude the potential influence of the dimethylamine ion (DMA^+) produced by the hydrolysis of DMF solvent under acidic conditions, we tested the ion migration speed of the cubic phase DMACl-doped $MAPbI_3$ film, and the results (Figure S24) showed that the ion migration effect was still significantly stronger than that of T-MPI. This indicated that the doping of DMA^+ is not the dominating factor in the improvement of the stability of T-MPI.

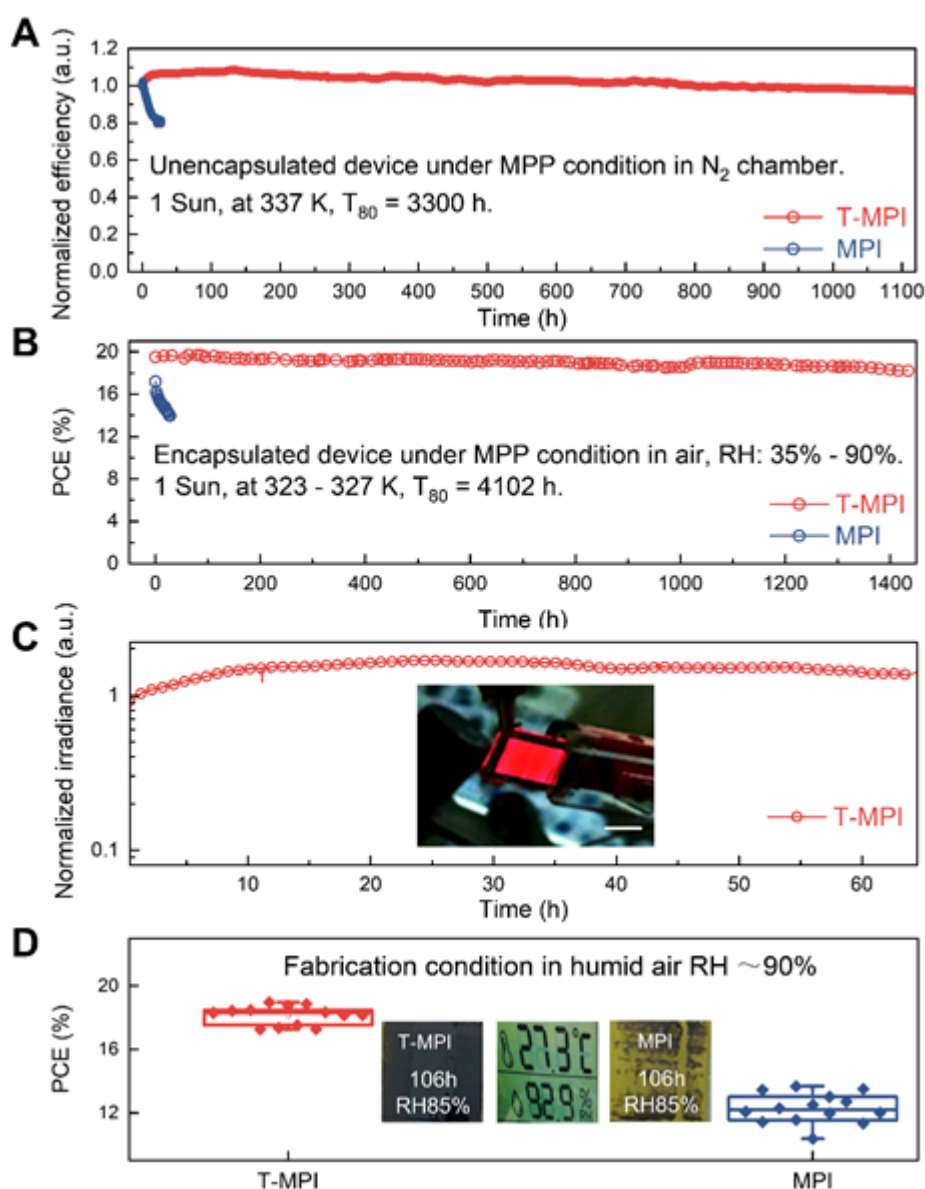


Figure 4. Device stability under extreme conditions.

(A) Long-term operational stability test of unencapsulated devices at continuous output at maximum power point (MPP) in nitrogen atmosphere under 100 mW/cm² LED light illumination with violet and red light followed the *ISOS-L-2I* protocol.^[48] (B) Long-term operational stability test of encapsulated devices at continuous output at MPP in air without humidity control (RH: 35%-90%) under 100 mW/cm² LED light illumination with violet and red light enhanced referred to the *ISOS-L-3* protocol.^[48] (C) Solar cell-structured LED operational stability test under constant current (30 mA/cm²) mode. The inset image showed

bright and uniform electroluminescence (EL) on a 1 cm×1.3 cm large area solar cell-structured LED under a bias of 1.3 V. Scale bar, 1 cm. (D) Statistical parameters of PCE for SFTSQ without passivation layer and referenced blade coating device prepared under 90% relative humidity. The inset picture showed the enhanced high-humidity storage stability of T-MPI film compared to the MPI film.

The T-MPI devices also showed excellent thermal-shocking stability due to the eliminating phase transition and surface compressive strain as well as high crystallinity. Thermal cycling stability of PSC was measured by continuous cycle between 358 K and 258 K with a sharp temperature variation rate of 60 K/min (Figure 3G). As predicted, the regular PSCs cannot withstand thermal-shocking and the efficiency greatly attenuated just after the first cycle (Figure S25). In a strong contrast, the T-MPI devices showed no conspicuous attenuation on each parameter even after 36 hours' continuous multiple thermal-shocking cycles.

Most encouragingly, highly stable PSCs achieved based on MAPbI₃ composition, with more than ~98.6% initial efficiency retained after more than 1000 h continuous operation at maximum power point (MPP) under one-sun illumination (Figure 4A) at nitrogen and an estimated T₈₀ exceeding 3300 h, which was much higher than that of 27 h in control MAPbI₃ device. The temperature of the samples was not intentionally controlled and was measured to be around 337 K during continuous operation. In order to further simulate the actual working environment of the device, we also tested the operational stability of the encapsulated device at MPP condition under one-sun illumination in the air (relative humidity: 35-90%, temperature: 323-328 K). Excellent stability with T₈₀ up to 4102 h is also realized by SFTSQ process (Figure 4B). MA⁺ is generally considered to be less stable and cause strong ion migration effect,^[8] the breakthrough of operational stability in efficient MA-based PSCs without further GBs or interfacial passivation is an excellent proof that the inhibition of ion migration in T-MPI devices benefiting from the regulation of local and global strain.

The stability after adding the interface layer is also tested to examine the ion stability of the device under a larger electric field and the compatibility of surface compressive strain and interface layer. The results showed that the device working as an LED also exhibited extraordinary irradiance stability in the constant current (30 mA/cm²) mode and the irradiance maintained 82% of the highest brightness after 60 h continuous operation without cooling (Figure 4C), which approaching one of the best stability of perovskite bifunctional device to the best of our knowledge. Furthermore, bright and uniform light emitting can be seen on a 1 cm×1.3 cm large area device under a low bias of 1.3 V, which further proved the high film uniformity, repeatability and scalability of the T-MPI devices.

It is worth noting that, the SFTSQ process enabled a high throughput of PSCs in air-condition without being affected by ambient moisture and temperature (Figure S26), benefiting from the high materials stability and the post-annealing-free fabrication process without requirement of glovebox and oven. The film morphology and device performance hardly changed with or without post-annealing (Figure S27-29). Moreover, the T-MPI showed excellent tolerance to moisture with highly reliable devices reproducibility, even when PSCs were fabricated in air under relative humidity (RH) up to 90% (Figure 4D, Figure S30-31), presenting unique potentials for low cost high-throughput photovoltaics fabrication.

3. Conclusion

In conclusion, highly stable T-MPI with compressed surface lattice structure was fabricated via non-equilibrium scalable SFTSQ process making the ion migration activation energy significantly improved, which provided a new pathway to regulate the intrinsic ionic nature of perovskite. Both high efficiency and stability were achieved in MA-based PSC with a power conversion efficiency (PCE) up to 22.99% and long-term operational stability with T_{80} lifetime exceeding 4000 hours. The T-MPI devices showed dramatically enhanced

intrinsic stability for bias, moisture, long-term operation, high temperature, anti-thermal-shock, even though in MA-based perovskite.

Acknowledgments: Funding: This work was supported by the National Natural Science Foundation of China (No.22179050, No.21875089, No. 21827805). **Author contributions:** Q.D. conceived the idea. Q.D supervised the work. Y.K. and A.W. fabricated the devices and conducted the characterization. Y.K. contributed the devices and stability characterization. Y.K., Y.S and R.L. contributed to the ionic stability characterization. X.W. and L.Z. contributed to the data processing, calculation and simulation. R.L., A.W., W.X. conducted the nanoindentation and TRPL measurement. H.L. provides advice and assistance in LED related characterization. Q.D., Y.K., A.W. and R.L. wrote the manuscript. **Competing interests:** None declared. **Data and materials availability:** All (other) data needed to evaluate the conclusions in the paper are present in the paper or the supplementary materials.

References

- [1] H. Lu, Y. Liu, P. Ahlawat, A. Mishra, W. R. Tress, F. T. Eickemeyer, Y. Yang, F. Fu, Z. Wang, C. E. Avalos, B. I. Carlsen, A. Agarwalla, X. Zhang, X. Li, Y. Zhan, S. M. Zakeeruddin, L. Emsley, U. Rothlisberger, L. Zheng, A. Hagfeldt, M. Gratzel, Science 2020, 370, eabb8985.
- [2] G. Kim, H. Min, K. S. Lee, D. Y. Lee, S. M. Yoon, S. I. Seok, Science 2020, 370, 108.
- [3] J. J. Yoo, G. Seo, M. R. Chua, T. G. Park, Y. Lu, F. Rotermund, Y. K. Kim, C. S. Moon, N. J. Jeon, J. P. Correa-Baena, V. Bulovic, S. S. Shin, M. G. Bawendi, J. Seo, Nature 2021, 590, 587.
- [4] J. Jeong, M. Kim, J. Seo, H. Lu, P. Ahlawat, A. Mishra, Y. Yang, M. A. Hope, F. T. Eickemeyer, M. Kim, Y. J. Yoon, I. W. Choi, B. P. Darwich, S. J. Choi, Y. Jo, J. H. Lee, B. Walker, S. M. Zakeeruddin, L. Emsley, U. Rothlisberger, A. Hagfeldt, D. S. Kim, M. Gratzel, J. Y. Kim, Nature 2021, 592, 381.

-
- [5] H. Min, D. Y. Lee, J. Kim, G. Kim, K. S. Lee, J. Kim, M. J. Paik, Y. K. Kim, K. S. Kim, M. G. Kim, T. J. Shin, S. I. Seok, *Nature* 2021, 598, 444.
- [6] X. K. Liu, W. Xu, S. Bai, Y. Jin, J. Wang, R. H. Friend, F. Gao, *Nat Mater* 2021, 20, 10.
- [7] H. Wu, Y. Ge, G. Niu, J. Tang, *Matter* 2021, 4, 144.
- [8] B.-w. Park, H. W. Kwon, Y. Lee, D. Y. Lee, M. G. Kim, G. Kim, K.-j. Kim, Y. K. Kim, J. Im, T. J. Shin, S. I. Seok, *Nature Energy* 2021, 6, 419.
- [9] J. Li, R. Xia, W. Qi, X. Zhou, J. Cheng, Y. Chen, G. Hou, Y. Ding, Y. Li, Y. Zhao, X. Zhang, *Journal of Power Sources* 2021, 485.
- [10] A. Mei, Y. Sheng, Y. Ming, Y. Hu, Y. Rong, W. Zhang, S. Luo, G. Na, C. Tian, X. Hou, Y. Xiong, Z. Zhang, S. Liu, S. Uchida, T.-W. Kim, Y. Yuan, L. Zhang, Y. Zhou, H. Han, *Joule* 2020, 4, 2646.
- [11] Y. Wang, Z. Zhang, Y. Lan, Q. Song, M. Li, Y. Song, *Angew Chem Int Ed Engl* 2021, 60, 8673.
- [12] Y. Shao, Y. Fang, T. Li, Q. Wang, Q. Dong, Y. Deng, Y. Yuan, H. Wei, M. Wang, A. Gruverman, J. Shield, J. Huang, *Energy & Environmental Science* 2016, 9, 1752.
- [13] P. Holzhey, P. Yadav, S.-H. Turren-Cruz, A. Ummadisingu, M. Grätzel, A. Hagfeldt, M. Saliba, *Materials Today* 2019, 29, 10.
- [14] G. Xia, B. Huang, Y. Zhang, X. Zhao, C. Wang, C. Jia, J. Zhao, W. Chen, J. Li, *Adv Mater* 2019, 31, e1902870.
- [15] W. Zhou, Y. Zhao, X. Zhou, R. Fu, Q. Li, Y. Zhao, K. Liu, D. Yu, Q. Zhao, *J Phys Chem Lett* 2017, 8, 4122.
- [16] T. Zhang, C. Hu, S. Yang, *Small Methods* 2019, 4.
- [17] S. Yang, S. Chen, E. Mosconi, Y. Fang, X. Xiao, C. Wang, Y. Zhou, Z. Yu, J. Zhao, Y. Gao, F. De Angelis, J. Huang, *Science* 2019, 365, 473.
- [18] J. S. Yun, J. Seidel, J. Kim, A. M. Soufiani, S. Huang, J. Lau, N. J. Jeon, S. I. Seok, M. A. Green, A. Ho-Baillie, *Advanced Energy Materials* 2016, 6.
- [19] B. Chen, J. Song, X. Dai, Y. Liu, P. N. Rudd, X. Hong, J. Huang, *Adv Mater* 2019, e1902413.
- [20] Y. Lin, B. Chen, Y. Fang, J. Zhao, C. Bao, Z. Yu, Y. Deng, P. N. Rudd, Y. Yan, Y. Yuan, J. Huang, *Nat Commun* 2018, 9, 4981.

-
- [21] H. Fan, F. Li, P. Wang, Z. Gu, J. H. Huang, K. J. Jiang, B. Guan, L. M. Yang, X. Zhou, Y. Song, *Nat Commun* 2020, 11, 5402.
- [22] Y. Song, W. Bi, A. Wang, X. Liu, Y. Kang, Q. Dong, *Nat Commun* 2020, 11, 274.
- [23] C. Liang, H. Gu, Y. Xia, Z. Wang, X. Liu, J. Xia, S. Zuo, Y. Hu, X. Gao, W. Hui, L. Chao, T. Niu, M. Fang, H. Lu, H. Dong, H. Yu, S. Chen, X. Ran, L. Song, B. Li, J. Zhang, Y. Peng, G. Shao, J. Wang, Y. Chen, G. Xing, W. Huang, *Nature Energy* 2020.
- [24] S. H. Turren-Cruz, A. Hagfeldt, M. Saliba, *Science* 2018, 362, 449.
- [25] S. Bai, P. Da, C. Li, Z. Wang, Z. Yuan, F. Fu, M. Kawecki, X. Liu, N. Sakai, J. T. Wang, S. Huettnner, S. Buecheler, M. Fahlman, F. Gao, H. J. Snaith, *Nature* 2019, 571, 245.
- [26] Y. Wang, T. Wu, J. Barbaud, W. Kong, D. Cui, H. Chen, X. Yang, L. Han, *Science* 2019, 365, 687.
- [27] F. Li, X. Deng, F. Qi, Z. Li, D. Liu, D. Shen, M. Qin, S. Wu, F. Lin, S.-H. Jang, J. Zhang, X. Lu, D. Lei, C.-S. Lee, Z. Zhu, A. K. Y. Jen, *Journal of the American Chemical Society* 2020.
- [28] D. Liu, D. Luo, A. N. Iqbal, K. W. P. Orr, T. A. S. Doherty, Z. H. Lu, S. D. Stranks, W. Zhang, *Nat Mater* 2021, 20, 1337.
- [29] M. Wang, Z. Ni, X. Xiao, Y. Zhou, J. Huang, *Chemical Physics Reviews* 2021, 2.
- [30] N. Li, X. Niu, Q. Chen, H. Zhou, *Chem Soc Rev* 2020, 49, 8235.
- [31] G. Li, T. Zhang, Y. Zhao, *Journal of Materials Chemistry A* 2015, 3, 19674.
- [32] J. Pan, C. Mu, Q. Li, W. Li, D. Ma, D. Xu, *Adv Mater* 2016, 28, 8309.
- [33] L. Yang, J. Wang, W. W. Leung, *ACS Appl Mater Interfaces* 2015, 7, 14614.
- [34] L. Zeng, S. Chen, K. Forberich, C. J. Brabec, Y. Mai, F. Guo, *Energy & Environmental Science* 2020, 13, 4666.
- [35] X. Zheng, Y. Hou, C. Bao, J. Yin, F. Yuan, Z. Huang, K. Song, J. Liu, J. Troughton, N. Gasparini, C. Zhou, Y. Lin, D.-J. Xue, B. Chen, A. K. Johnston, N. Wei, M. N. Hedhili, M. Wei, A. Y. Alsalloum, P. Maity, B. Turedi, C. Yang, D. Baran, T. D. Anthopoulos, Y. Han, Z.-H. Lu, O. F. Mohammed, F. Gao, E. H. Sargent, O. M. Bakr, *Nature Energy* 2020, 5, 131.
- [36] G. Zheng, C. Zhu, J. Ma, X. Zhang, G. Tang, R. Li, Y. Chen, L. Li, J. Hu, J. Hong, Q. Chen, X. Gao, H. Zhou, *Nat Commun* 2018, 9, 2793.

-
- [37] Y. Ma, P. M. Hangoma, W. I. Park, J. H. Lim, Y. K. Jung, J. H. Jeong, S. H. Park, K. H. Kim, *Nanoscale* 2018, 11, 170.
- [38] J. Zhao, Y. Deng, H. Wei, X. Zheng, Z. Yu, Y. Shao, J. E. Shield, J. Huang, *Sci Adv* 2017, 3, eaao5616.
- [39] Y. Yao, Z. Huang, P. Xie, S. D. Lacey, R. J. Jacob, H. Xie, F. Chen, A. Nie, T. Pu, M. Rehwoldt, D. Yu, M. R. Zachariah, C. Wang, R. Shahbazian-Yassar, J. Li, L. Hu, *Science* 2018, 359, 1489.
- [40] H. Min, M. Kim, S. U. Lee, H. Kim, G. Kim, K. Choi, J. H. Lee, S. I. Seok, *Science* 2019, 366, 749.
- [41] S. F. Solari, L. N. Poon, M. Worle, F. Krumeich, Y. T. Li, Y. C. Chiu, C. J. Shih, *J Am Chem Soc* 2022, 144, 5864.
- [42] A. Jamshaid, Z. Guo, J. Hieulle, C. Stecker, R. Ohmann, L. K. Ono, L. Qiu, G. Tong, W. Yin, Y. Qi, *Energy & Environmental Science* 2021.
- [43] J. Yu, M. Wang, S. Lin, *ACS Nano* 2016, 10, 11044.
- [44] M. A. Reyes-Martinez, A. L. Abdelhady, M. I. Saidaminov, D. Y. Chung, O. M. Bakr, M. G. Kanatzidis, W. O. Soboyejo, Y. L. Loo, *Adv Mater* 2017, 29.
- [45] W. Pan, H. Wu, J. Luo, Z. Deng, C. Ge, C. Chen, X. Jiang, W.-J. Yin, G. Niu, L. Zhu, L. Yin, Y. Zhou, Q. Xie, X. Ke, M. Sui, J. Tang, *Nature Photonics* 2017, 11, 726.
- [46] W. Q. Wu, Z. Yang, P. N. Rudd, Y. Shao, X. Dai, H. Wei, J. Zhao, Y. Fang, Q. Wang, Y. Liu, Y. Deng, X. Xiao, Y. Feng, J. Huang, *Sci Adv* 2019, 5, eaav8925.
- [47] M. I. Saidaminov, J. Kim, A. Jain, R. Quintero-Bermudez, H. Tan, G. Long, F. Tan, A. Johnston, Y. Zhao, O. Voznyy, E. H. Sargent, *Nature Energy* 2018, 3, 648.
- [48] M. V. Khenkin, E. A. Katz, A. Abate, G. Bardizza, J. J. Berry, C. Brabec, F. Brunetti, V. Bulović, Q. Burlingame, A. Di Carlo, R. Cheacharoen, Y.-B. Cheng, A. Colmann, S. Cros, K. Domanski, M. Dusza, C. J. Fell, S. R. Forrest, Y. Galagan, D. Di Girolamo, M. Grätzel, A. Hagfeldt, E. von Hauff, H. Hoppe, J. Kettle, H. Köbler, M. S. Leite, S. Liu, Y.-L. Loo, J. M. Luther, C.-Q. Ma, M. Madsen, M. Manceau, M. Matheron, M. McGehee, R. Meitzner, M. K. Nazeeruddin, A. F. Nogueira, Ç. Odabaşı, A. Osherov, N.-G. Park, M. O. Reese, F. De Rossi, M. Saliba, U. S. Schubert, H. J. Snaith, S. D. Stranks, W. Tress, P. A. Troshin, V. Turkovic, S. Veenstra, I. Visoly-Fisher, A. Walsh, T. Watson, H. Xie, R. Yıldırım, S. M. Zakeeruddin, K. Zhu, M. Lira-Cantu, *Nature Energy* 2020, 5, 35.

- [49] L. Wang, H. Zhou, J. Hu, B. Huang, M. Sun, B. Dong, G. Zheng, Y. Huang, Y. Chen, L. Li, Z. Xu, N. Li, Z. Liu, Q. Chen, L. D. Sun, C. H. Yan, *Science* 2019, 363, 265.
- [50] Q. Chen, H. Zhou, Y. Fang, A. Z. Stieg, T. B. Song, H. H. Wang, X. Xu, Y. Liu, S. Lu, J. You, P. Sun, J. McKay, M. S. Goorsky, Y. Yang, *Nat Commun* 2015, 6, 7269.
- [51] X. Zheng, B. Chen, J. Dai, Y. Fang, Y. Bai, Y. Lin, H. Wei, Xiao C. Zeng, J. Huang, *Nature Energy* 2017, 2.
- [52] O. Dupré, R. Vaillon, M. A. Green, *Solar Energy Materials and Solar Cells* 2015, 140, 92.
- [53] M. V. Lee, S. R. Raga, Y. Kato, M. R. Leyden, L. K. Ono, S. Wang, Y. Qi, *Journal of Materials Research* 2016, 32, 45.
- [54] U.-G. Jong, C.-J. Yu, Y.-M. Jang, G.-C. Ri, S.-N. Hong, Y.-H. Pae, *Journal of Power Sources* 2017, 350, 65.
- [55] A. E. Williams, P. J. Holliman, M. J. Carnie, M. L. Davies, D. A. Worsley, T. M. Watson, *J. Mater. Chem. A* 2014, 2, 19338.
- [56] H. Chen, Q. Wei, M. I. Saidaminov, F. Wang, A. Johnston, Y. Hou, Z. Peng, K. Xu, W. Zhou, Z. Liu, L. Qiao, X. Wang, S. Xu, J. Li, R. Long, Y. Ke, E. H. Sargent, Z. Ning, *Adv Mater* 2019, 31, e1903559.

Table of contents (ToC):

Here we show a highly crystalline perovskite with compressed surface lattice-structure can be made by a thermal-shocking fabrication, which significantly enhances the ionic activation temperature and contributes to hysteresis-free operation of perovskite solar cells (PSCs) at high temperature up to 363 K, enabling efficient and stable PSCs fabricated by a high-speed post-annealing-free process in air with a scalable bar-coating technique.

